Published March 21, 2016

Laser microsurgery reveals conserved viscoelastic behavior of the kinetochore

Gheorghe Cojoc,[1]* Emanuele Roscioli,[2]* Lijuan Zhang,[3] Alfonso García-Ulloa,[1] Jagesh V. Shah,[4] Michael W. Berns,[5] Nenad Pavin,[6] Daniela Cimini,[2] Iva M. Tolić,[1,7] and Juraj Gregan[3]

[1]Max Planck Institute of Molecular Cell Biology and Genetics, 01307 Dresden, Germany
[2]Department of Biological Sciences and Biocomplexity Institute, Virginia Polytechnic Institute and State University, Blacksburg, VA 24061
[3]Max F. Perutz Laboratories, Department of Chromosome Biology, University of Vienna, 1030 Vienna, Austria
[4]Department of Systems Biology, Harvard Medical School, Boston, MA 02115
[5]Beckman Laser Institute and University of California, Irvine, Irvine, CA 92612
[6]Department of Physics, Faculty of Science, University of Zagreb, 10000 Zagreb, Croatia
[7]Division of Molecular Biology, Ruđer Bošković Institute, 10000 Zagreb, Croatia

Accurate chromosome segregation depends on proper kinetochore–microtubule attachment. Upon microtubule interaction, kinetochores are subjected to forces generated by the microtubules. In this work, we used laser ablation to sever microtubules attached to a merotelic kinetochore, which is laterally stretched by opposing pulling forces exerted by microtubules, and inferred the mechanical response of the kinetochore from its length change. In both mammalian PtK1 cells and in the fission yeast *Schizosaccharomyces pombe*, kinetochores shortened after microtubule severing. Interestingly, the inner kinetochore–centromere relaxed faster than the outer kinetochore. Whereas in fission yeast all kinetochores relaxed to a similar length, in PtK1 cells the more stretched kinetochores remained more stretched. Simple models suggest that these differences arise because the mechanical structure of the mammalian kinetochore is more complex. Our study establishes merotelic kinetochores as an experimental model for studying the mechanical response of the kinetochore in live cells and reveals a viscoelastic behavior of the kinetochore that is conserved in yeast and mammalian cells.

Introduction

The function of many biological systems is known to depend on the mechanical properties of the system components. For instance, it is widely acknowledged that the mechanical properties of muscle cells dictate muscle function and that certain molecular components of connective tissues confer the elasticity necessary to react to mechanical stress without rupturing. Whereas physiology approaches have been used for many years to study the mechanics of living tissues, studying the mechanical properties of subcellular structures has been a more challenging endeavor. Nevertheless, it is believed that the mechanical properties of certain subcellular structures are important for proper cellular function, and in recent years, several investigators have used cell biology and biophysics approaches to study such properties. For instance, biophysical approaches have been used to study the mechanical properties of mitotic apparatus components, including chromosomes (Poirier et al., 2000; Sun et al., 2011) and spindles (Gatlin et al., 2010; Shimamoto et al., 2011). Moreover, recent studies suggested that the mechanical properties of kinetochores (KTs) and the underlying centromeric chromatin may be important for several KT functions, including establishment of correct attachment of KTs to microtubules (MTs), correction of erroneous KT attachments, chromosome congression, and chromosome segregation (Loncarek et al., 2007; Maresca and Salmon, 2009; Uchida et al., 2009; Akiyoshi et al., 2010; Stephens et al., 2011, 2013; Dumont et al., 2012; Umbreit et al., 2014). It is particularly important to analyze such KT properties in the context of live cells, where KT behavior is determined not only by its intrinsic mechanical properties but also by multiple KT-independent factors. Here, we used anaphase merotelic KTs as an experimental model to investigate the mechanical response of eukaryotic KTs upon release of the pulling forces exerted by MTs. Merotelic KTs are attached to MTs emanating from both spindle poles and, during anaphase, become laterally stretched by opposing

*G. Cojoc and E. Roscioli contributed equally to this paper.

Correspondence to Juraj Gregan: gregan@fns.uniba.sk; Iva M. Tolić: tolic@irb.hr; or Daniela Cimini: cimini@vt.edu

G. Cojoc's present address is Biotechnology Center, Technische Universität Dresden, 01307 Dresden, Germany.

E. Roscioli's present address is Division of Biomedical Sciences, Warwick Medical School, University of Warwick, CV4 7AL Coventry, England, UK.

L. Zhang's present address is Advanced Microscopy, Vienna Biocenter Core Facilities GmbH, 1030 Vienna, Austria.

J. Gregan's present address is Dept. of Genetics, Faculty of Natural Sciences, Comenius University, 84215 Bratislava, Slovak Republic.

Abbreviations used in this paper: KT, kinetochore; MT, microtubule; NOC, nocodazole.

The Rockefeller University Press $30.00
J. Cell Biol.
www.jcb.org/cgi/doi/10.1083/jcb.201506011

Published March 21, 2016

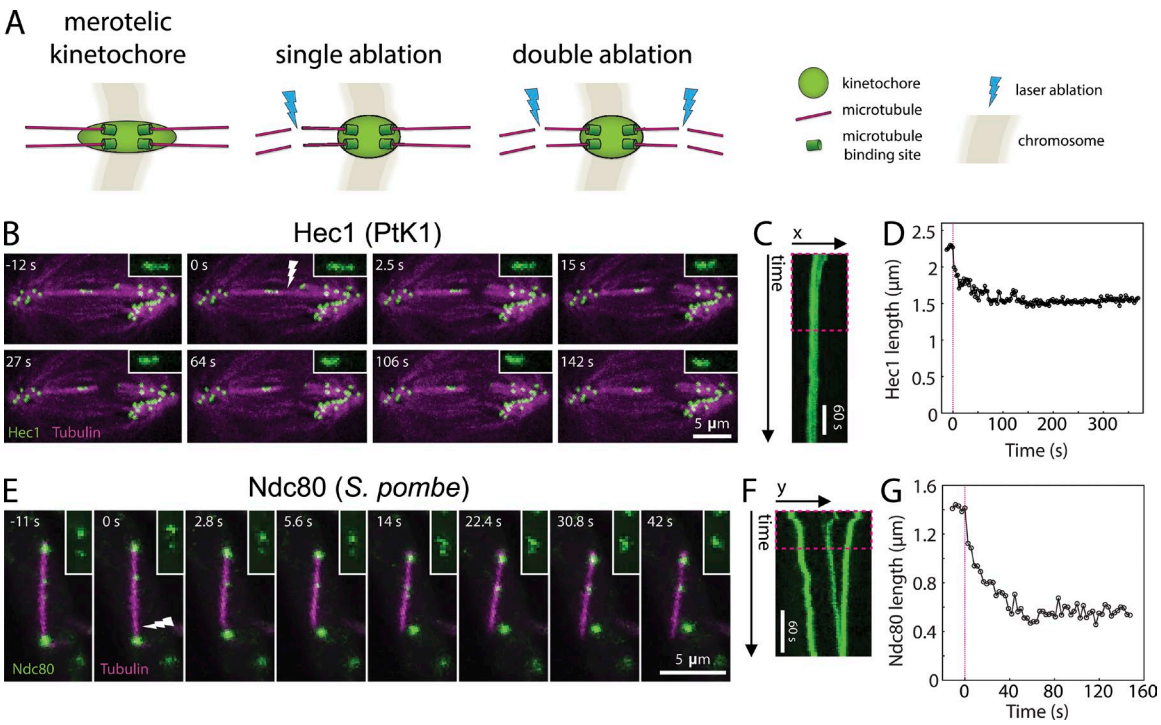

Figure 1. **Merotelic KTs shorten after MT severing.** (A) Diagrammatic representation of the in vivo assay in which MTs attached to a merotelic KT are severed by laser. Laser ablation was used to sever one (single ablation) or both (double ablation) MT bundles attached to a merotelic KT in anaphase cells, releasing the forces acting on the KT. Change of the KT length after laser severing reflects its mechanical response. (B) Maximum intensity projection of time-lapse images of a merotelic KT (Hec1-GFP, green) in a PtK1 cell and the severing of one of the two MT bundles (α-tubulin–X-Rhodamine, magenta). Time 0 indicates the frame before ablation. The white lightning sign indicates the ablation site. Images were acquired with a time resolution Δt = 2.5 s. Close-up views show lagging KTs (2×). (C) Time projection of the area containing the merotelic KT from the cell in B. The boxed region indicates the time interval shown in B. (D) Relaxation kinetics of the merotelic KT from B and C. The red dashed line indicates the severing time. (E) Maximum intensity projections of time-lapse images of a merotelic KT (Ndc80-GFP, green) in a *S. pombe* cell and the severing (lightning sign) of the spindle (α-tubulin–mCherry, magenta) close to one spindle pole body. The time 0 is the frame before ablation. The spindle breakage occurred immediately after ablation. Images were acquired with a time resolution Δt = 2.8 s. Close-up views show lagging KTs (1.35×). (F) Time projection of an area containing the merotelic KT from the cell in E. The boxed region indicates the time interval shown in E. (G) Relaxation kinetics of the merotelic KT from E and F. The red dashed line indicates the severing time.

pulling forces exerted by the bound MTs (Khodjakov et al., 1997; Cimini et al., 2001; Gregan et al., 2007). In our assay, we released the pulling forces acting on the merotelic KT by laser severing of attached MTs (Fig. 1 A) and examined the dynamics by which KT length changed. The mechanical properties of the KT were then interpreted by using two simple theoretical models that took into account the kinetics of KT length changes.

Results and discussion

Stretched KTs progressively shorten after MT severing in both PtK1 cells and fission yeast

We first analyzed mammalian PtK1 cells stably expressing outer KT component Hec1 fused to GFP (Hec1-GFP), released from nocodazole to increase the frequency of merotelic attachments (Cimini et al., 2001) and microinjected during prometaphase with X-rhodamine–labeled tubulin to visualize the spindle. Once cells reached anaphase, we selected those displaying merotelically attached KTs and used a focused laser beam to sever one of the two MT bundles attached to the stretched merotelic KT (Fig. 1 A, single ablation). Depolymerization of MT plus ends at the site of ablation indicated successful MT severing (Fig. S1 A). Cells were imaged every 2–5 s for 5–10 min, and the changes in KT length upon release of the pulling forces were analyzed. We found that upon successful ablation, stretched KTs typically shortened gradually after severing of the K-fiber (Fig. 1, B–D; Video 1; and see Fig. S2 A for mean trace data and Fig. S1, C and D, for less frequent types of response). Recent studies found more rapid relaxation times of the distance between sister KTs after laser severing of K-fibers in metaphase cells (Elting et al., 2014; Sikirzhytski et al., 2014). However, it is difficult to compare our data with the data from those studies because of the substantially different experimental setups (i.e., anaphase merotelic KTs vs. metaphase chromosomes). This difference in relaxation times could be due to various causes, including considerably lower stretch of individual KTs in metaphase than that observed for anaphase merotelic KTs and the presence of centromeric sister-chromatid cohesion in metaphase cells.

In experiments in which MT severing was not successful and only photobleaching occurred, KT length did not change, suggesting that the irradiation caused by the laser does not affect KT morphology (Fig. S2 A). Overall, the observation that the KT shortens after the forces are released is a signature of its elastic properties, whereas the slowdown in shortening reflects its viscous properties (Figs. 1 D and S2 A; Meyers and Chawla, 2009). Thus, we conclude that the outer KT domain of PtK1 cells exhibits a viscoelastic behavior upon release of the pulling forces exerted by one of the two attached MT bundles.

To determine whether mechanical response of the KT is evolutionary conserved, we performed similar experiments in

Published March 21, 2016

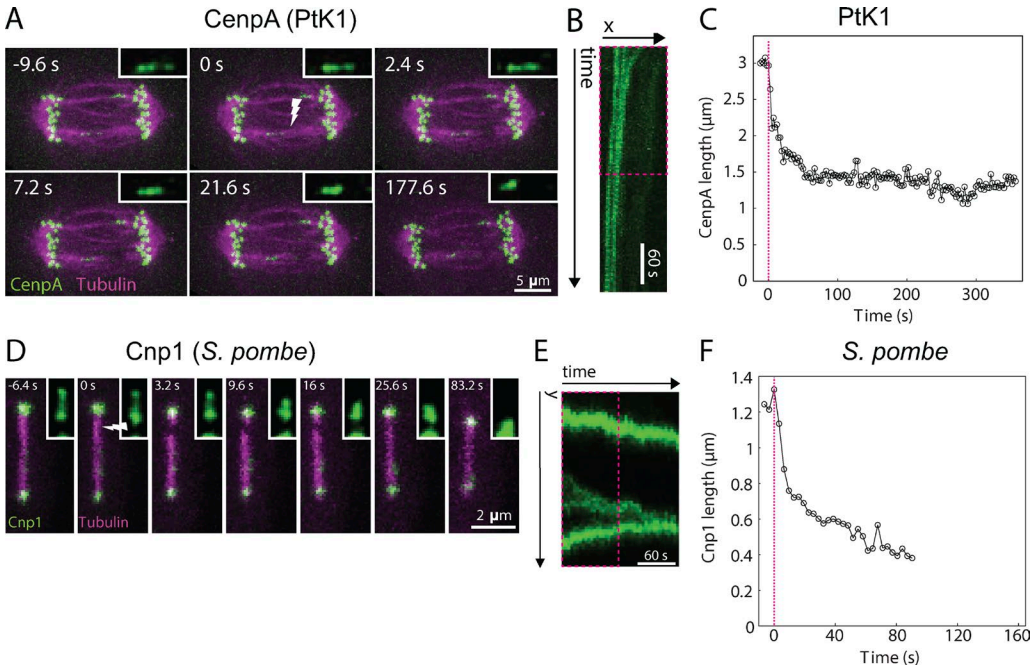

Figure 2. **Shortening of the inner KT/centromere after MT severing.** (A) Maximum intensity projections of a merotelic KT in PtK1 cells expressing GFP-CenpA (green) and injected with α-tubulin–X-rhodamine (magenta). Time 0 indicates the frame before ablation. The white lightning sign indicates the ablation site. Images were acquired with a time resolution Δt = 2.4 s. Close-up views show lagging KTs (1.85×). (B) Time projection of the area containing the merotelic KT from the cell in A. The boxed region indicates the time interval shown in A. (C) Relaxation kinetics of the merotelic KT from A and B. The red dashed line indicates the severing time. (D) Maximum intensity projections of a merotelic KT in fission yeast cell expressing Cnp1-GFP, shown in green, and α-tubulin–mCherry, shown in magenta. The white lightning sign indicates the ablation site. The time 0 is the frame before ablation. The spindle breakage occurred immediately after ablation. Images were acquired with a time resolution Δt = 3.2 s. Close-up views show lagging KTs (1.5× magnification). (E) Time projection of an area containing the merotelic KT from the cell in D. The boxed region indicates the time interval shown in D. (F) Relaxation kinetics of the merotelic KT from D and E. The red dashed line indicates the severing time.

the fission yeast *Schizosaccharomyces pombe*. We performed our experiments in *pcs1Δ* mutant cells, which exhibit high frequencies of lagging chromosomes because of merotelic attachment (Gregan et al., 2007; Rumpf et al., 2010) and used Ndc80-GFP and mCherry-Atb2 to visualize the outer KT and MTs, respectively. To distinguish whether the lagging KT signal in *S. pombe* anaphase cells was a single KT or two/few adjacent KTs, we quantified the relative KT signal intensity (Materials and methods; Courtheoux et al., 2009). As described for PtK1 cells (see previous two paragraphs), we used a laser to sever K-fibers. However, unlike in PtK1 cells, it was not possible to distinguish individual MT bundles attached to a merotelic KT. To ensure that we cut all MTs attached to the KT from one side, we severed all spindle MTs, which resulted in spindle breakage and inward movement of the spindle poles (Fig. S1 B), as previously described (Tolić-Nørrelykke et al., 2004; Raabe et al., 2009; Maghelli and Tolić-Nørrelykke, 2010, 2011). The merotelic KT moved poleward after MT severing, which was not the case in PtK1 cells. However, similarly to what we found in PtK1 cells, we observed a gradual decrease in KT length after MT severing (Fig. 1, E–G; Video 2; and see Fig. S2 B for mean trace data). Unsuccessful MT severing had only a minor effect on KT length (Fig. S2 B). Collectively, our results suggest that the viscoelastic behavior of the KT is evolutionarily conserved in both fission yeast and mammalian PtK1 cells.

The inner KT/centromere relaxes faster than the outer KT

The KT is a sophisticated molecular assembly composed of more than 80 proteins organized into two major domains, the outer and the inner KT, which interact with MTs and centromeric DNA, respectively (Santaguida and Musacchio, 2009). The viscoelastic response observed in our MT-severing experiments is likely to depend on the combined response of KT proteins and the underlying centromeric heterochromatin. Our previous analyses of merotelic KTs in fixed fission yeast showed that the outer KT domain is stretched more than the inner domain (Gregan et al., 2007). Similarly, we found that in fixed PtK1 cells, the KT domain defined by Hec1 was more stretched compared with the CenpA KT domain within the same anaphase merotelic KT (unpublished data). These observations suggest that the mechanical response of the outer KT and the inner KT/centromere upon release of the pulling forces exerted by MTs may also be different. Therefore, we decided to use the same MT-severing approach to characterize the mechanical behavior of the inner KT/centromere visualized by GFP-tagged CenpA/Cnp1 (PtK1/*S. pombe*). CenpA/Cnp1 is a histone-like protein found in nucleosomes within the centromeric DNA region. Thus, behavior of the GFP-tagged CenpA/Cnp1 reflects the combined properties of the inner KT domain and the underlying centromeric heterochromatin. Our analyses in live cells confirmed that in both fission yeast and PtK1 cells, the outer KT is stretched more than the inner KT/centromere (Fig. S2, D and E). Moreover, we found that the inner KT/centromere shortened gradually (Fig. 2, A–F; Videos 3 and 4; and Fig. 3). Thus, also in the case of the inner KT/centromere, the observed kinetics suggested a viscoelastic behavior. However, we found that the relaxation of the inner KT/centromere was faster than the relaxation observed for the outer KT (compare graphs in Fig. 2, C and F, with Fig. 1, D and G; see also Fig. 3), suggesting that the elastic component plays a more important role in the relaxation response of the inner KT/centromere compared with the outer KT. This

Published March 21, 2016

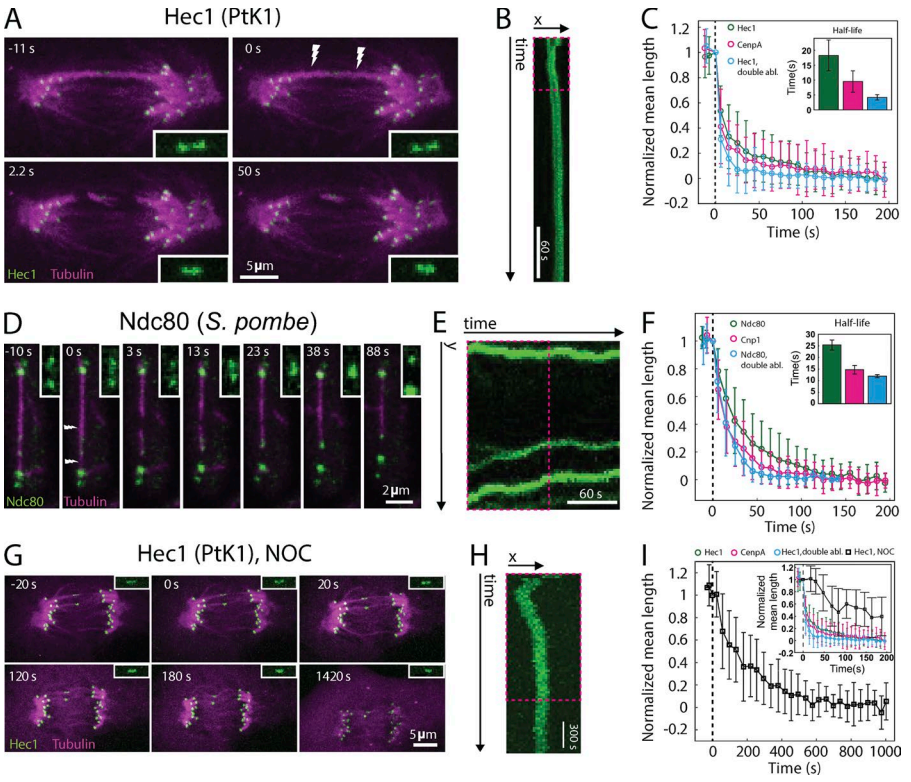

Figure 3. **Outer KT relaxation upon double ablation and 9 µM NOC treatment in PtK1 and fission yeast cells.** (A) Maximum intensity projections of a merotelic KT in PtK1 cell expressing Hec1-GFP, shown in green, and injected with α-tubulin–X-rhodamine, shown in magenta. Time 0 indicates the frame before ablation. The white lightning signs indicate ablation sites. Images were acquired with a time resolution Δt = 2.2 s. Close-up views show lagging KTs (2.5×). (B) Time projection of the area containing the merotelic KT from the cell in A. The boxed region indicates the time interval shown in A. (D) Maximum intensity projections of a merotelic KT in fission yeast cell expressed Ndc80-GFP, shown in green, and α-tubulin–mCherry, shown in magenta. The white lightning signs indicate ablation sites. The time 0 is the frame before ablation. The spindle breakage occurred immediately after ablation. Images were acquired with a time resolution Δt = 3 s. Close-up views show lagging KTs (1.65×). (E) Time projection of an area containing the merotelic KT from the cell in D. The boxed region indicates the time interval shown in D. (C and F) Normalized KT length as a function of time, for the inner (magenta) and outer (green) KT in PtK1 (C) and *S. pombe* cells (F) after single ablation. Normalized outer KT length as a function of time after double ablation is shown in light blue. Data for each KT were normalized setting the value before ablation to 1 and the minimum value reached by the individual KT to 0, binned, and averaged. Error bars represent standard deviation, $n = 25/18$ for Hec1/Ndc80 single ablation, $n = 15/24$ for CenpA/Cnp1 single ablation, and $n = 9/10$ for Hec1/Ndc80 double ablation. All the data were fitted with a single exponential equation, $L(t) = A \times \exp(-t \times \ln(2)/t1/2)$. Half-lives are shown in the insets. (G) Maximum intensity projections of a merotelic KT in PtK1 cell expressing Hec1-GFP, shown in green, and injected with α-tubulin–X-rhodamine, shown in magenta. Time 0 indicates the frame before addition of 9 µM NOC. Images were acquired with a time resolution Δt = 20s. Close-up views show lagging KTs (1.5×). (H) Time projection of an area containing the merotelic KT from the cell in panel G. The boxed region indicates the time interval shown in G. (I) Normalized KT length (outer KT) as a function of time. PtK1 cells were treated with 9 µM NOC. Comparison between ablation experiments and 9 µM NOC treatment for the first 200 s is shown in I (inset). The length change was initially slow (I, inset), most likely because of the slow kinetics of NOC-dependent MT depolymerization as compared with a sudden MT severing.

indicates that the chromatin, which has been shown to behave as an elastic material (Poirier et al., 2000; Bouck and Bloom, 2007; Sun et al., 2011), may have a strong influence on the mechanical response of the inner KT. Alternatively, factors external to the KT, such as residual pulling forces exerted by the residual MT stub that remains bound to the KT after laser ablation (Elting et al., 2014; Sikirzhytski et al., 2014), may differentially affect the behavior of the inner and outer KT. In cases in which MT severing was not successful, we observed only a minor effect on inner KT morphology immediately after laser ablation (Fig. S2 C).

We also observed that in fission yeast, stretched merotelic KTs occasionally relaxed independent of MT severing (Fig. S1, E and F). These events likely reflect correction of merotelic KT–MT attachment during anaphase. Importantly, the relaxation kinetics of these KTs was indistinguishable from those where we induced relaxation by MT severing (Fig. S2 F), suggesting that similar mechanisms drive KT shortening in both cases. In conclusion, our experiments indicate that inner KT/centromere and outer KT display similar viscoelastic response but different relaxation kinetics.

Insights into the different mechanical response of inner and outer KT

Because the outer KT domain (and particularly Hec1) is responsible for establishing MT attachment, we considered the possibility that the slower relaxation of the outer KT may depend on the pulling forces exerted by the unsevered MT bundle. To test this possibility, we performed ablations on both sides of the KT (double ablation experiments) in cells expressing GFP-tagged Hec1/Ndc80 (Fig. 1 A, double ablation; Fig. 3, A, B, D, and E; and Videos 5 and 6). We found that KT relaxation in both PtK1 and fission yeast cells was faster after double ablation compared with single ablation and that double ablation resulted in kinetics of Hec1/Ndc80 that were more similar to the kinetics of CenpA/Cnp1 after single ablation (Fig. 3, C and F). This suggests that the forces exerted by the unsevered MT bundle contribute to the slower shortening of the outer KT versus the inner KT/centromere.

Previous studies using EM tomography have shown that MTs are attached end-on to merotelic KTs (Khodjakov et al., 1997; Cimini et al., 2001). However, the orientation of the MTs with respect to the KT outer plate is different than that observed in metaphase. Indeed, MTs are positioned perpendicularly with respect to metaphase KTs. Instead, for most anaphase merotelic KTs, the MTs are oriented nearly parallel, although a few with nearly perpendicular orientation can be observed (Fig. S3, A and B). To determine whether these differences in MT orientation produced any difference in behavior, we compared two sets of KTs in which the bound MTs were oriented either perpendicularly or parallel. We found that there were only minor differences when we compared relaxation response of KTs with perpendicular or parallel orientation (Fig. S3, C–G).

Published March 21, 2016

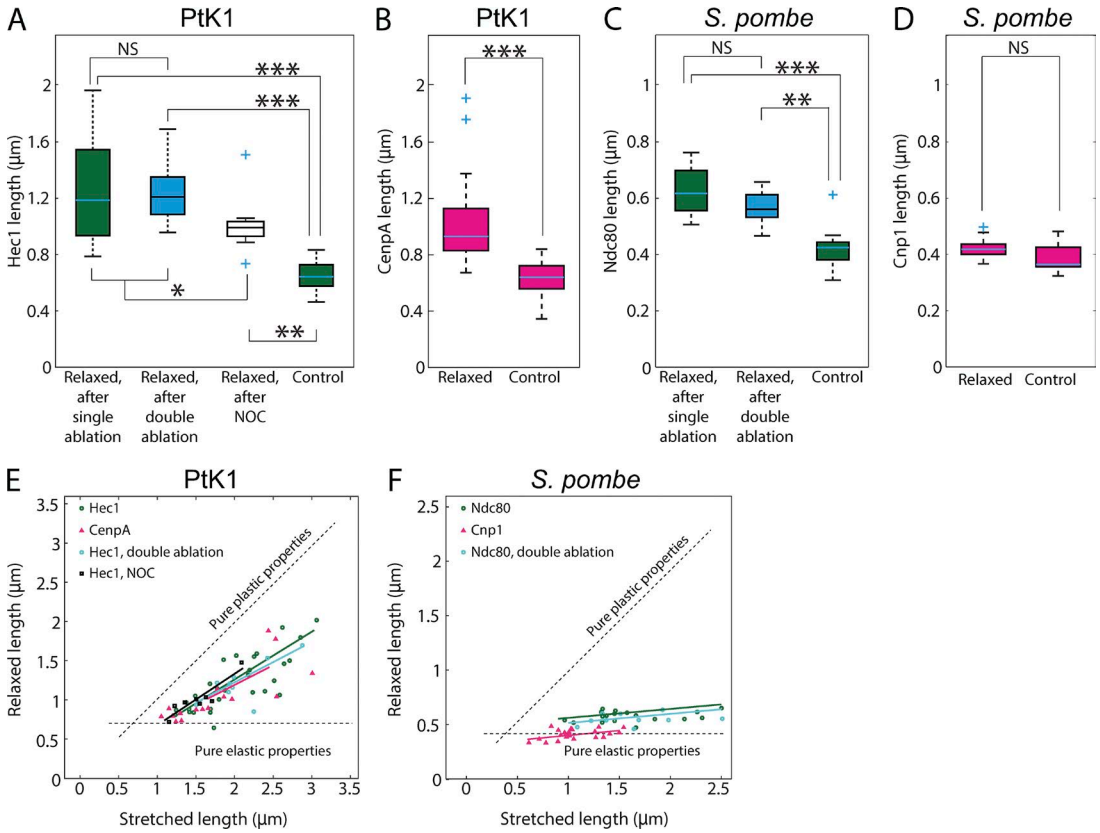

Figure 4. **KT relaxed length depends on the stretched length in PtK1 cells, but not in *S. pombe*.** (A–D) Comparison of the relaxed KT length after laser ablation, NOC treatment, and control unstretched KTs. As control KTs, we measured PtK1 anaphase KTs that were attached to a K-fiber emanating from only one spindle pole and *S. pombe* KTs that were not lagging during anaphase. Length of control KTs was determined by using automated software to detect the KT and to count pixels with KT-specific signal. These measurements are influenced by the imaging conditions and they may not represent the absolute length of KTs, but they can be used to compare merotelic and control KTs. Relaxed length after severing one K-fiber for the outer KT, Hec1/Ndc80, is shown in green and for inner KT, CenpA/Cnp1, in magenta. The relaxed length of the outer KT after severing both K-fibers is shown in blue. The relaxed length of KTs in PtK1 cells after 9-µM NOC treatment is shown in white. The lengths are calculated as mean of the values measured in the last 30 s and 15 s of the experiment for PtK1 cells and fission yeast, respectively. The tops and bottoms of each box are the 25% and 75% of the sample, respectively. The line in the middle of each box is the sample median. Hec1-single ablation, $n = 25$; Hec1-double ablation, $n = 9$; Hec1-NOC treatment, $n = 9$; Hec1-control KTs, $n = 43$; CenpA-ablation, $n = 15$; CenpA-control KTs, $n = 67$; Ndc80-single ablation, $n = 18$; Ndc80-double ablation, $n = 10$; Ndc80-control KTs, $n = 11$; Cnp1-ablation, $n = 24$; and Cnp1-control KTs, $n = 11$. There was a statistically significant difference between the relaxed and control KT length in all cases in A–C (**, $P < 0.001$; ***, $P < 0.0001$), but no significant difference (NS, $P > 0.05$) in D. NOC was added at 9-µM concentration for 15–25 min. (E and F) Correlation between initial stretched KT length and relaxed length. The initial stretched length was calculated as a mean of the values measured before ablation. Solid colored lines represent linear fit for each specific condition.

In previous experiments where K-fibers were cut at different distances from metaphase KTs, the centromeric chromatin relaxed less when the severing was performed further from the KT because of forces exerted by the MT stub that remained attached to the KT after MT severing (Kajtez et al., 2016). Similarly, Maiato et al. observed that K-fiber ablation did not reduce centromere stretch of metaphase chromosomes (Maiato et al., 2004a), yet when the ablation site was closer to the KT, the centromere relaxed (Elting et al., 2014; Sikirzhytski et al., 2014). To identify a possible correlation between KT relaxation kinetics and MT stub length in our assay, we plotted the relaxation times (half-life), the final length of the KT after ablation (relaxed length) and the difference between the initial and the final KT length (absolute and relative relaxation length) versus MT stub length. We found no significant correlation between KT relaxation characteristics and MT stub length (Fig. S2 G), but we cannot exclude the possibility that the absence of correlation may be caused by a small range of stub lengths. Interestingly, treatment of PtK1 cells with 9 µM nocodazole (NOC), which causes nearly complete MT depolymerization (a notable exception was the presence of MT stubs that remained attached to KTs after NOC treatment; Fig. 3 G), resulted in a small but significant decrease of the relaxed length of the outer KT domain in PtK1 cells as compared with relaxation by laser severing (Fig. 3, G–I; Fig. 4, A and E; and Video 7).

After MT severing, KTs exhibit residual stretching

As described in previous sections, we found that in both yeast and PtK1 cells the KT quickly relaxed upon release of the pulling forces exerted by MTs. Importantly, we observed that the fission yeast inner KT shortened close to the typical unstretched length within ~100–150 s after the pulling force was released via MT severing. In contrast, the yeast outer KT and especially PtK1 KTs (both inner and outer domains) shortened but did not regain the length typical of unstretched KTs (Fig. 4, A–D). We exclude the possibility that this is caused by the pulling forces exerted by the unsevered MT bundle, because the PtK1 and the yeast outer KTs failed to regain the initial unstretched length even after double ablation or 9 µM NOC treatment (Fig. 4,

Published March 21, 2016

A and C). One possible explanation is that the persisting KT stretch is caused by forces exerted by the MT stubs that remain attached to the KT after MT severing or NOC treatment. In addition, nonkinetochore MTs that interact laterally with the KT and that cannot be detected in our experimental setup may also contribute to the persisting KT stretch. However, another possibility is that this residual stretch may be caused by intrinsic plastic properties of the KT or permanent unraveling of the underlying centromeric chromatin.

We also explored the correlation between the stretched length and the relaxed length. In PtK1 cells, the relaxed length was larger for KTs that were stretched more (Fig. 4 E). Conversely, in fission yeast, the relaxed length was independent of the stretched length (Fig. 4 F). Both inner and outer KT domains showed the same qualitative behavior in each of the two cell types (Fig. 4, E and F).

Simple viscoelastic models suggest differences in KT mechanical structure in PtK1 and *S. pombe* cells

Our experimental data suggest that the KT behaves as a viscoelastic material both in PtK1 and fission yeast cells. However, in PtK1 cells, but not in fission yeast, the more stretched KTs remain more stretched after severing. We set out to explain our observations by considering simple models of viscoelastic materials. A minimal representation of a viscoelastic material includes a Hookean spring characterized by a spring constant and a linear dashpot characterized by a drag coefficient. The spring and the dashpot can be connected either in series, which is known as the Maxwell model (Fig. 5 A), or in parallel, which is known as the Voigt model (Fig. 5 B).

The two models can be distinguished by their characteristic response to force. We consider a simple case of constant force acting for a certain period of time (Fig. 5, C and D; and see Materials and methods), although forces acting on the KT may change during anaphase (Rago and Cheeseman, 2013). In the Maxwell model, when the force is removed, the object relaxes immediately to a new relaxed length, which is larger for objects that were stretched more before the force was removed (Fig. 5, C and E). On the contrary, in the Voigt model, when the force is removed, the object relaxes gradually to its original relaxed length (Fig. 5, D and F). Thus, a qualitative difference between these models can be used to identify the model relevant for KTs in PtK1 and fission yeast cells.

Our experiments showed that in PtK1 cells, the relaxed length was larger for KTs that were stretched more (Fig. 4 E). Conversely, fission yeast KTs relaxed to a length close to the length of control KTs, irrespective of how much they were initially stretched (Fig. 4 F). These findings suggest that the behavior of the KT in PtK1 cells is closer to the Maxwell model (compare Figs. 4 E and 5 E), whereas the fission yeast KT is closer to the Voigt model (compare Figs. 4 F and 5 F).

Our experiments also showed that KT relaxation was gradual both in PtK1 and fission yeast cells, being slower in yeast (Fig. 3, C and F). Thus, the Voigt model explains not only the extent of relaxation but also the relaxation kinetics of fission yeast KTs (compare Fig. 3 F and Fig. 5 D). However, the Maxwell model does not explain the relaxation kinetics of PtK1 KTs (compare Fig. 3 C and Fig. 5 C), even though it does explain the extent of their relaxation, as discussed in previous paragraphs. A combination of the Maxwell and the Voigt model could explain the complete response of PtK1 KTs, suggesting that the

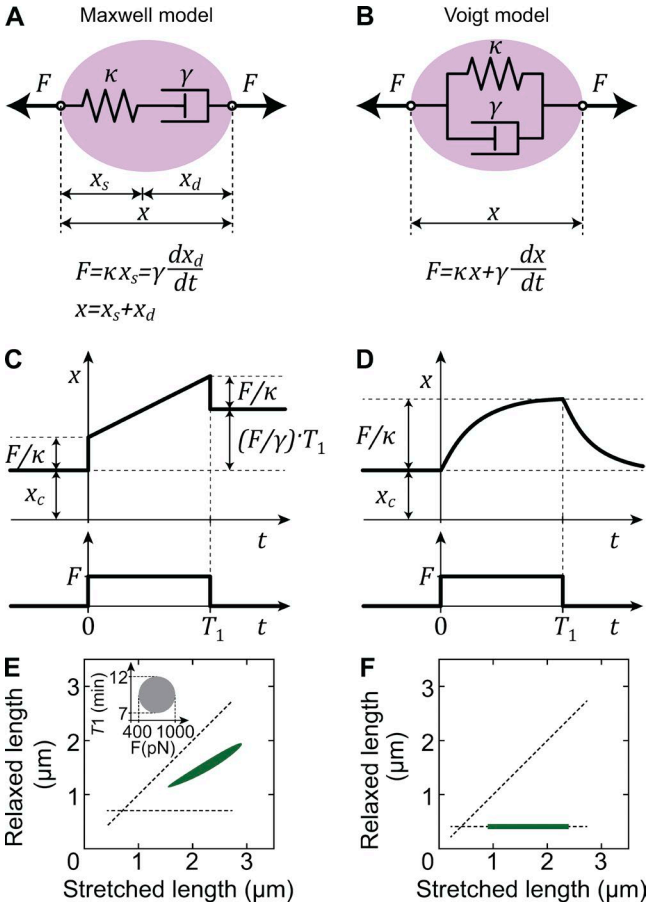

Figure 5. **Two simple models of a KT as a viscoelastic object consisting of a spring and a dashpot.** (A and B) Schematic representation of the models. A spring of a stiffness κ and a dashpot of a viscous drag coefficient γ are connected in series (A) or in parallel (B). The KT (pink ellipse) is under tension *F* and has a length *x*. In A, the length is the sum of the length of the spring, x_s, and the length of the dashpot, x_d. The equations of the models are given under the schemes. (C and D) KT length as a function of time for the models in A and B, respectively, for a constant tension *F* that starts to act at time $t = 0$ and stops at $t = T_1$. The length of a control KT is denoted x_c. (E and F) Relaxed length as a function of the stretched length (dark green) for the models in A and B, respectively. In E, $\gamma = 5 \times 10^5$ pNs/μm, $\kappa = 1{,}000$ pN/μm, and $x_c = 0.7$ μm, whereas *F* and *t* were varied simultaneously in the intervals $F = 400$–$1{,}000$ pN and $T1 = 7$–12 min, as shown in the inset. In F, $\kappa = 100$ pN/μm, $x_c = 0.4$ μm, and *F* was varied in the interval 50–200 pN. Horizontal and oblique dashed lines correspond to complete relaxation to the control length x_c and no relaxation, respectively.

mechanical structure of the mammalian KT is more complex than that of the yeast KT.

Our simple models provide additional testable predictions. The Maxwell model predicts that the KT length increases at a constant rate upon exertion of MT pulling forces (Fig. 5 C). Conversely, the Voigt model predicts that the extended KT length cannot exceed a certain maximum value and that the time required for achieving this maximum stretch is similar to the time required for relaxation (Fig. 5 D). Although it would be interesting to test these predictions by measuring the kinetics of stretching of merotelic KTs in the two model systems, this may be technically difficult because of the challenge of identifying merotelic KTs before anaphase onset.

In summary, our study establishes merotelic KTs as an experimental system for studying the mechanical response of the KT in live cells and describes a viscoelastic response of the

Published March 21, 2016

KT upon release of the pulling forces exerted by MTs that is conserved in both yeast and mammalian cells. Our experimental assay is unique in that we were able to exploit a force being applied by the cell itself and release such force nearly instantaneously by laser ablating MT bundles attached to an anaphase merotelic KT. Using anaphase KTs allowed us to analyze properties of a single KT independent of the sister KT/chromatid, which may affect KT behavior in metaphase. This also enabled us to analyze the mechanical response of the KT in its native environment, where both mechanical properties of the KT as well as KT-independent factors determine KT behavior. Several studies suggested that the mechanical properties of KTs may be important for KT functions including establishment of correct attachment of KTs to MTs and faithful chromosome segregation (Loncarek et al., 2007; Maresca and Salmon, 2009; Uchida et al., 2009; Akiyoshi et al., 2010; Stephens et al., 2011, 2013; Dumont et al., 2012; Umbreit et al., 2014). We therefore believe that the viscoelastic response of the merotelic KT characterized in this study is relevant to processes that involve properly attached KTs. Future studies should be aimed at identifying KT components that provide these viscoelastic properties and determine the physiological relevance of the KT viscoelastic behavior. Our work thus opens new lines of research including studies of how cells can use the KT mechanical properties to prevent and repair merotelic KT attachments, how kinetochore mechanical properties may contribute to metaphase and anaphase KT function, and how meiosis-specific KT alterations affect KT properties.

Materials and methods

Generation of Hec1-GFP and GFP-CenpA PtK1 cell lines

PtK1 cells stably expressing fluorescently tagged human Hec1 or PtK1 CenpA were produced through the transduction of retroviral particles according to the instructions for high-titer retrovirus production provided by Takara Bio Inc. The EGFP-N1 plasmid carrying the *HEC1* gene was a gift from J. DeLuca (Colorado State University, Fort Collins, CO). In brief, the *HEC1-EGFP* gene was initially subcloned into the XhoI and NotI sites of the pLNCX2 retroviral vector (Takara Bio Inc.) that harbors the Ψ packaging sequence. The PtK2 *CENP-A* gene was cloned and initially inserted into mCherry vector for N-terminal tagging (pJag456). We used BglII and SalI restriction sites to subclone the PtK2 *CENP-A* gene into the pRetroQ-AcGFP1-C1 retroviral vector (Takara Bio Inc.), also harboring the Ψ packaging sequence. To produce high-efficiency retroviral particles, we transfected the packaging GP2-293 cells (Takara Bio Inc.), carrying the viral *gag* and *pol* genes, with the pLNCX2-*HEC1-EGFP* plasmid or the pRetroQ-AcGFP1-*CENP-A* together with the VSV-G vector (Takara Bio Inc.) that provided the viral envelope gene (*env*). The resulting retroviral particles were used to infect PtK1 cells that were subsequently placed under selection in Geneticin- or Puromycin-containing media to respectively obtain the Hec1-GFP PtK1 and the GFP-CenpA PtK1 cell lines used in this study.

Cell culture

Hec1-GFP PtK1 and GFP-CenpA PtK1 cells were grown in Ham's F12 medium (Invitrogen) supplemented with 1% sodium pyruvate (Invitrogen), 1% antibiotic/antimycotic (Invitrogen), and 10% fetal bovine serum (Invitrogen) and maintained at 37°C in a humidified CO_2 incubator. For experiments, cells were grown in 35-mm glass-bottom MatTek dishes for 24 or 48 h before observation. During time-lapse imaging, Ham's F12 medium was replaced with phenol red–free L-15 medium supplemented with 4.5 g/l glucose (Sigma-Aldrich), 1% antibiotic/antimycotic (Invitrogen), and 10% fetal bovine serum (Invitrogen).

Generation of *S. pombe* strains

JM2595 (*h⁻ kanMX6-Pcnp1-mEGFP-cnp1 ade6-M210 leu1-32 ura4-D18*) strain (provided by J.Q. Wu, The Ohio State University, Columbus, OH) was crossed with JG16070 (*h⁺ mCherry-atb2-hph leu1-32, ura4-D18*) to generate JG16573 (*h⁺ kanMX6-Pcnp1-mEGFP-cnp1 mCherry-atb2-hph leu1-32, ura4-D18*). To delete the *pcs1⁺* gene, JG16573 was transformed with the plasmid p17, resulting in JG16633 (*h⁺ kanMX6-Pcnp1-mEGFP-cnp1 mCherry-atb2-hph pcs1::natMX4 leu1-32, ura4-D18*).

FY14794 (*h⁹⁰ ade6-216 leu1-32 lys1-131 ura4-D18 ndc80::ndc80-GFP-HA-kan*) was crossed with JG16070 (*h⁺ mCherry-atb2-hph leu1-32, ura4-D18*) to generate JG16559 (*h⁺ ndc80::ndc80-GFP-HA-kan mCherry-atb2-hph leu1-32, ura4-D18*). To delete the *pcs1⁺* gene, JG16559 was transformed with the plasmid p17, resulting in JG16621 (*h⁺ ndc80::ndc80-GFP-HA-kan mCherry-atb2-hph pcs1::natMX4 leu1-32, ura4-D18*).

Sample preparation: PtK1

Merotelic attachments were induced using a NOC washout protocol. A 6.6 mM stock solution of nocodazole (Sigma-Aldrich) in DMSO (Sigma-Aldrich) was diluted into Ham's F12 medium to a final concentration of 3 µM, which was used to treat the cells for ∼60–90 min. For MT visualization, a 0.5-µg/µl final concentration of X-rhodamine–labeled tubulin in injection buffer (20 mM Hepes, 100 mM KCl, and 1 mM DTT in H_2O) was used. Microinjection was performed during the NOC treatment, using the semiautomatic mode of a microinjector (InjectMan NI 2; Eppendorf). To prevent tubulin polymerization inside of the needle, microinjection was performed at room temperature. Once injected, the NOC was washed out and the cells were incubated at 37°C for ∼15 min before starting the observation.

Cells in which the MT bundles attached to the merotelic KT were not severed but depolymerized were treated with 9 µM NOC for 15–25 min once they reached anaphase and the merotelic KT was clearly visible.

Sample preparation: yeast

S. pombe strains were grown overnight (14–16 h) on yeast extract media (YE5S) agar plates with supplements (adenine, leucine, uracil, histidine, and arginine) at 25°C. For manipulation and imaging, fresh cells were resuspended in liquid Edinburgh minimal medium with adenine, leucine, uracil, histidine, and arginine (EMM5S) and transferred to the base of a 35-mm Petri dish (MatTek Corporation) coated with 2 µl of 2-mg/ml lectin (Sigma-Aldrich). Free cells were removed by washing with EMM5S, and the Petri dish was filled with 300 µl EMM5S and covered with a coverslip sealed with silicone (GE Bayer Silicones). Cell manipulation and imaging was performed at 25°C in a Bachhoffer chamber (Tempcontrol 37–2 digital; ZEISS).

Microscopy and image acquisition: PtK1

Two inverted confocal microscopes were used for imaging and MT severing in PtK1 cells. First, we used NLO microscope (LSM 710; ZEISS) and a Plan Apochromat 63×/1.40 oil differential interference contrast objective (ZEISS), the inverted version of the (LSM 780; ZEI SS) used for experiments in yeast. Both ZEISS microscopes were operated with Zen Black software 2011. GFP fluorescence was excited with a 488-nm line of a multiline argon-ion laser (LASOS) and a primary dichroic mirror (DM 488/561). For X-rhodamine excitation, we used a diode-pumped 561-nm solid-state laser. GFP and X-rhodamine

Published March 21, 2016

emission were detected in the range of 490–570 and 570–735 nm, respectively. No images were taken during the laser ablation. Time-lapse Z-stacks of ∼15 optical sections, with a 500-nm z-distance, were taken at 3.5- to 6.5-s intervals using unidirectional scanning. The images have an *xy* pixel size of 150–215 nm.

MT bundle severing was performed using a single Ti:Sa femtosecond pulsed laser (Chameleon Vision II; Coherent), tuned to a wavelength of 800 nm and a theoretical pulse duration of 140 fs at 80 MHz. The beam was coupled to the bleaching port of the NLO laser-scanning microscope (LSM 710). The light path of the pulsed laser was different from the path of the imaging one. The pulsed laser light was reflected onto the objective by a long pass dichroic mirror LP690. For a maximum output power of 3030 mW corresponding to 100% of the laser, the measured power before the objective was 1,053 mW (using a Coherent power meter). The estimated power at the sample, corresponding to a 35–50% range of the maximum output power, was ∼37–53 mW. The objective transmission at 800 nm is ∼10%. MT bundle severing was achieved by scanning the laser, over a user-defined region of interest, for ∼50–80 ms total exposure time. This corresponds to a total energy ∼1.9–4.3 mJ. The ablation was performed as close as possible to the KT to avoid the effect previously reported by Maiato et al. (2004b) that ablations of K-fiber at sites distant from the KT did not reduce the centromere stretch.

Cells were also imaged and manipulated using an inverted microscope (IX71; Olympus) with a back illuminated EMCCD camera (iXon 897; Andor Technology) with 16-µm pixel size, a spinning-disc scan head (CSU10; Yokogawa Electric Corporation) equipped with a fast piezo objective z-positioner (PIFOC; Physik Instrumente GmbH & K.G.), and a UPlanSApo 100×/1.4 NA oil objective (Olympus). iQ software 3.0 (Andor Technology) was used to operate the acquisition, camera, and piezo stage. GFP and X-Rhodamine fluorescence were excited at 488 and 561 nm, respectively. Images were acquired at 1.9- to 2.6-s time intervals. The laser intensity was controlled using the acousto-optic tunable filter inside the Revolution Laser Combiner (ALC; Andor Technology). The emission wavelength was selected using respective emission filters BL 525/30 (Semrock) and ET 605/70 (Chroma) mounted in a fast, motorized filter wheel (Lambda-10B; Sutter Instrument). The images have an *xy* pixel size of 168 nm.

MT bundle severing was performed using a MicroPoint (ALC; Andor Technology) with 408-nm dye resonator cell.

Microscopy and image acquisition: yeast

Time-lapse images of live cells were taken with an infinity-corrected optics NLO upright microscope (LSM 780) with infinity-corrected optics and a Plan-Apochromat 63–/1.40 oil differential interference contrast objective (ZEISS). GFP was excited with a 488 nm line of a multiline argon-ion laser (LASOS) and a primary dichroic mirror DM 488/561. For mCherry excitation, we used a diode-pumped 561-nm solid-state laser. GFP and mCherry emissions were detected using an internal GaAsP detector (Hamamatsu Photonics) in the range of 490–570 nm and 580–680 nm, respectively. No images were acquired during laser ablation. Time-lapse Z-stacks of 8–11 optical sections, with a 500-nm z-distance, were taken at 2.5- to 5-s intervals using unidirectional scanning. Images have an *xy* pixel size of 90–135 nm.

MT/spindle severing was performed using a single Ti:Sa femtosecond pulsed laser (Chameleon Vision II; Coherent), tuned to a wavelength of 745 nm and a theoretical pulse duration of 140 fs at 80 MHz. The beam was coupled to the bleaching port of the NLO laser-scanning microscope (LSM 780). The light path of the pulsed laser was different from the path of the imaging one. The pulsed laser light was reflected onto the objective by a long pass dichroic mirror LP690. For a maximum output power of 2,480 mW corresponding to 100% of the laser, the measured power before the objective was 857 mW (using a Coherent power meter). The estimated power at the sample, corresponding to a 20–30% range of the maximum output power, was ∼20–30 mW. The objective transmission at 745 nm is 12%. MT severing was achieved by scanning the laser, over a user-defined region of interest, for ∼40–60-ms total exposure time. This corresponds to a total energy ∼0.8–1.8 mJ.

KT tracking

Stretched KT ends were tracked using an ImageJ plugin, Low Light Tracking Tool (Fig. S3 H; http://fiji.sc/Low_Light_Tracking_Tool; Krull et al., 2014). KT lengths were obtained by calculating the distance between the two KT ends using MatLAB (The MathWorks).

Size of control KTs was determined by using a custom automated ImageJ routine to detect and count pixels with KT-specific signal (Fig. S3 I). Channel of GFP-tagged KTs was separated, Z-projected, and loaded (Fig. S3 I, second image) into Fiji plugin. By creating a profile plot of the KTs and their surrounding region, the initial background threshold and neighborhood threshold of what is considered to be the control KT was set. The working image was scanned and, at each pixel, the mean neighborhood value was computed, and then its intensity value and the mean neighborhood value were compared with both thresholds conditions. If one of them was not met, the pixel state would be set to 0; otherwise, 1. According to this, the working image would display the marked pixels (Fig. S3 I, third image) while running the algorithm. At this point, lines that indicate the KTs to be measured and the orientation of the measurement (Fig. S3 I, fourth image) could be drawn.

To distinguish a single KT from two/several adjacent KTs in *S. pombe*, the following method was used. The total KT signal along the spindle was measured using the ImageJ tool, Plot profile. The background was subtracted. The datasets were exported to MatLAB (The Mathworks), where a ratio of the lagging KT signal between SPBs and the total signal along the spindle was calculated. Assuming that each cell has six KTs, the ratio of 1:6 was considered a single KT.

Models of KT relaxation

Maxwell model: spring and dashpot connected in series. The total length of the system consisting of a spring with extension x_s and a dashpot with extension x_d, which are connected in series, reads $x = x_s + x_d$ (Fig. 5 A). In this system, both mechanical elements are under tension F. For the spring characterized by a spring constant κ and the dashpot characterized by a drag coefficient γ, the respective force-balance equations read:

$$F = \kappa x_s, \tag{1}$$

and

$$F = \gamma \frac{dx_d}{dt}. \tag{2}$$

We solve Eqs. 1 and 2 by considering three time intervals: (a) for time $t < 0$, the tensile force is zero ($F = 0$); (b) for time $0 < t < T_1$, the tensile force F is constant; and (c) for time $t < T_1$, the tensile force vanishes again (Fig. 5 C, bottom). In (a), the extensions of the spring and the dashpot are 0, giving the total extension for the system $x = 0$ (Fig. 5 C). In (b), the extension of the spring has a constant value:

$$x_s = \frac{F}{\kappa},$$

whereas the extension of the dashpot increases linearly with time:

$$x_d = \frac{F}{\gamma} t,$$

Published March 21, 2016

giving the total length

$$x = \frac{F}{\kappa} + \frac{F}{\gamma} t.$$

In (c), the extension of the spring relaxes to $x_s = 0$, and the extension of the dashpot has a constant value

$$x_d = \frac{F}{\gamma} T_1.$$

Thus, the total length is

$$x = \frac{F}{\gamma} T_1.$$

If the system has an initial length x_c, the total length is given as $x + x_c$ (Fig. 5 C).

Voigt model: spring and dashpot connected in parallel. When connected in parallel, the spring and the dashpot have the same extension, $x \equiv x_s = x_d$ (Fig. 5 B), and the force balance reads

$$F = \kappa x + \gamma \frac{dx}{dt}. \quad (3)$$

As in the case for the serial connection, we solve Eq. 3 for the same three time intervals (Fig. 5 D, bottom). In the time interval (a), the total extension of the system is $x = 0$ (Fig. 5 D). In the time interval (b), the total extension of the system obeys

$$x = \frac{F}{\kappa}(1 - e^{-\kappa t/\gamma}).$$

In the time interval (c), the total extension of the system relaxes, obeying

$$x = \frac{F}{\kappa}(1 - e^{-\kappa T_1/\gamma}) e^{-\kappa t/\gamma}.$$

If the system has an initial length x_c, the total length is given as $x + x_c$ (Fig. 5 D).

Estimation of parameters

For PtK1 cells, we assume that the force acting on the KT is in the range of 400–1,000 pN, based on the previously measured value of 700 pN for nonmerotelic KTs in anaphase (Nicklas, 1983). We assume that this force was acting on the KT for 7–12 min, which corresponds to the time between the initial stretching of the merotelic KT and our MT severing late in anaphase. By using these values for force and time, together with the spring constant $\kappa = 1{,}000$ pN/µm and the drag coefficient $\gamma = 5 \times 10^5$ pNs/µm, the Maxwell model reproduces the relationship between the relaxed and the stretched length measured for the PtK1 outer KT (Fig. 4 E). In particular, the parameters κ and γ were chosen in such a way that the theoretical data matched the experimental data (compare Fig. 4 E and Fig. 5 E).

For fission yeast KTs, we use the assumption that the force at the KT depends on the number of attached MTs, which is on average 25 in PtK1 cells (McDonald et al., 1992) and 2–4 in fission yeast (Ding et al., 1993). Thus, we assume that the force acting on the merotelic KT in fission yeast is roughly eight times lower than in PtK1 cells, i.e., in the range of 50–200 pN. By using these values in the Voigt model, we find that for a spring constant value $\kappa = 100$ pN/µm, the model reproduces the measured relationship between the relaxed and the stretched length of the outer KT (compare Fig. 4 F and Fig. 5 F). By using the experimentally measured relaxation time value for the outer KT, half-life = 25 s (Fig. 3 F), we obtain the drag coefficient $\gamma = 3{,}600$ pNs/µm.

Online supplemental material

Fig. S1 shows indications of successful MT severing in PtK1 and fission yeast cells and KT behavior observed after successful or unsuccessful MT severing. Fig. S2 shows normalized KT length observed after successful or unsuccessful MT severing, comparison of outer KT and inner KT/centromere stretch, kinetics of relaxation for KTs that were repaired spontaneously, and effect of MT stub length on KT relaxation. Fig. S3 shows comparison of relaxation response of KTs with perpendicular or parallel MT attachments and a scheme of KT tracking. Video 1 shows single ablation in PtK1 cells expressing Hec1-GFP. Video 2 shows single ablation in *S. pombe* cells expressing Ndc80-GFP. Video 3 shows single ablation in PtK1 cells expressing GFP-CenpA. Video 4 shows single ablation in *S. pombe* cells expressing Cnp1-GFP. Video 5 shows double ablation in PtK1 cells expressing Hec1-GFP. Video 6 shows double ablation in *S. pombe* cells expressing Ndc80-GFP. Video 7 shows PtK1 cells expressing Hec1-GFP treated with NOC. Online supplemental material is available at http://www.jcb.org/cgi/content/full/jcb.201506011/DC1. Additional data are available in the JCB DataViewer at http://dx.doi.org/10.1083/jcb.201506011.dv.

Acknowledgments

We thank the Max Planck Institute of Molecular Cell Biology and Genetics Light Microscopy Facility, N. Maghelli, and the Research Institute of Molecular Pathology for help with experimental setups; A. Krull for the tracking software; G. Civelekoglu-Scholey, T. Franzmann, and members of the Tolić and Cimini groups for helpful discussions; W.J. Qiu and J. DeLuca for sharing material; and I. Šarić for help with figures.

This work was supported by Human Frontier Science Program grant RGY0069/2010 to J. Gregan, D. Cimini, and I.M. Tolić. Additional support was provided by National Science Foundation grants MCB-0842551 and MCB-1517506 to D. Cimini. J.V. Shah was supported by a Beckman Laser Institute Faculty Fellowship. J. Gregan was supported by the following grants from the Austrian Science Fund: P21437 and P23609, EC (PCIG11-GA-2012-322300), APVV (APVV-0334-12), and VEGA (1/0196/14).

The authors declare no competing financial interests.

Submitted: 2 June 2015
Accepted: 25 February 2016

References

Akiyoshi, B., K.K. Sarangapani, A.F. Powers, C.R. Nelson, S.L. Reichow, H. Arellano-Santoyo, T. Gonen, J.A. Ranish, C.L. Asbury, and S. Biggins. 2010. Tension directly stabilizes reconstituted kinetochore-microtubule attachments. *Nature.* 468:576–579. http://dx.doi.org/10.1038/nature09594

Bouck, D.C., and K. Bloom. 2007. Pericentric chromatin is an elastic component of the mitotic spindle. *Curr. Biol.* 17:741–748. http://dx.doi.org/10.1016/j.cub.2007.03.033

Cimini, D., B. Howell, P. Maddox, A. Khodjakov, F. Degrassi, and E.D. Salmon. 2001. Merotelic kinetochore orientation is a major mechanism of aneuploidy in mitotic mammalian tissue cells. *J. Cell Biol.* 153:517–527. http://dx.doi.org/10.1083/jcb.153.3.517

Courtheoux, T., G. Gay, Y. Gachet, and S. Tournier. 2009. Ase1/Prc1-dependent spindle elongation corrects merotely during anaphase in fission yeast. *J. Cell Biol.* 187:399–412. http://dx.doi.org/10.1083/jcb.200902093

Ding, R., K.L. McDonald, and J.R. McIntosh. 1993. Three-dimensional reconstruction and analysis of mitotic spindles from the yeast, Schizosaccharomyces pombe. *J. Cell Biol.* 120:141–151. http://dx.doi.org/10.1083/jcb.120.1.141

Dumont, S., E.D. Salmon, and T.J. Mitchison. 2012. Deformations within moving kinetochores reveal different sites of active and passive force generation. *Science.* 337:355–358. http://dx.doi.org/10.1126/science.1221886

Elting, M.W., C.L. Hueschen, D.B. Udy, and S. Dumont. 2014. Force on spindle microtubule minus ends moves chromosomes. *J. Cell Biol.* 206:245–256. http://dx.doi.org/10.1083/jcb.201401091

Gatlin, J.C., A. Matov, G. Danuser, T.J. Mitchison, and E.D. Salmon. 2010. Directly probing the mechanical properties of the spindle and its matrix. *J. Cell Biol.* 188:481–489. http://dx.doi.org/10.1083/jcb.200907110

Gregan, J., C.G. Riedel, A.L. Pidoux, Y. Katou, C. Rumpf, A. Schleiffer, S.E. Kearsey, K. Shirahige, R.C. Allshire, and K. Nasmyth. 2007. The kinetochore proteins Pcs1 and Mde4 and heterochromatin are required to prevent merotelic orientation. *Curr. Biol.* 17:1190–1200. http://dx.doi.org/10.1016/j.cub.2007.06.044

Kajtez, J., A. Solomatina, M. Novak, B. Polak, K. Vukušić, J. Rüdiger, G. Cojoc, A. Milas, I. Šumanovac Šestak, P. Risteski, et al. 2016. Overlap microtubules link sister k-fibres and balance the forces on bi-oriented kinetochores. *Nat. Commun.* 7:10298. http://dx.doi.org/10.1038/ncomms10298

Khodjakov, A., R.W. Cole, B.F. McEwen, K.F. Buttle, and C.L. Rieder. 1997. Chromosome fragments possessing only one kinetochore can congress to the spindle equator. *J. Cell Biol.* 136:229–240. http://dx.doi.org/10.1083/jcb.136.2.229

Krull, A., A. Steinborn, V. Ananthanarayanan, D. Ramunno-Johnson, U. Petersohn, and I.M. Tolić-Nørrelykke. 2014. A divide and conquer strategy for the maximum likelihood localization of low intensity objects. *Opt. Express.* 22:210–228. http://dx.doi.org/10.1364/OE.22.000210

Loncarek, J., O. Kisurina-Evgenieva, T. Vinogradova, P. Hergert, S. La Terra, T.M. Kapoor, and A. Khodjakov. 2007. The centromere geometry essential for keeping mitosis error free is controlled by spindle forces. *Nature.* 450:745–749. http://dx.doi.org/10.1038/nature06344

Maghelli, N., and I.M. Tolić-Nørrelykke. 2010. Optical trapping and laser ablation of microtubules in fission yeast. *Methods Cell Biol.* 97:173–183. http://dx.doi.org/10.1016/S0091-679X(10)97010-6

Maghelli, N., and I.M. Tolić-Nørrelykke. 2011. Laser ablation of the microtubule cytoskeleton: setting up and working with an ablation system. *Methods Mol. Biol.* 777:261–271. http://dx.doi.org/10.1007/978-1-61779-252-6_19

Maiato, H., J. DeLuca, E.D. Salmon, and W.C. Earnshaw. 2004a. The dynamic kinetochore-microtubule interface. *J. Cell Sci.* 117:5461–5477. http://dx.doi.org/10.1242/jcs.01536

Maiato, H., C.L. Rieder, and A. Khodjakov. 2004b. Kinetochore-driven formation of kinetochore fibers contributes to spindle assembly during animal mitosis. *J. Cell Biol.* 167:831–840. http://dx.doi.org/10.1083/jcb.200407090

Maresca, T.J., and E.D. Salmon. 2009. Intrakinetochore stretch is associated with changes in kinetochore phosphorylation and spindle assembly checkpoint activity. *J. Cell Biol.* 184:373–381. http://dx.doi.org/10.1083/jcb.200808130

McDonald, K.L., E.T. O'Toole, D.N. Mastronarde, and J.R. McIntosh. 1992. Kinetochore microtubules in PTK cells. *J. Cell Biol.* 118:369–383. http://dx.doi.org/10.1083/jcb.118.2.369

Meyers, M.A., and K.K. Chawla. 2009. Mechanical behavior of materials. Second edition. Cambridge University Press, Cambridge, UK. 882 pp.

Nicklas, R.B. 1983. Measurements of the force produced by the mitotic spindle in anaphase. *J. Cell Biol.* 97:542–548. http://dx.doi.org/10.1083/jcb.97.2.542

Poirier, M., S. Eroglu, D. Chatenay, and J.F. Marko. 2000. Reversible and irreversible unfolding of mitotic newt chromosomes by applied force. *Mol. Biol. Cell.* 11:269–276. http://dx.doi.org/10.1091/mbc.11.1.269

Raabe, I., S.K. Vogel, J. Peychl, and I.M. Tolić-Nørrelykke. 2009. Intracellular nanosurgery and cell enucleation using a picosecond laser. *J. Microsc.* 234:1–8. http://dx.doi.org/10.1111/j.1365-2818.2009.03142.x

Rago, F., and I.M. Cheeseman. 2013. Review series: The functions and consequences of force at kinetochores. *J. Cell Biol.* 200:557–565. http://dx.doi.org/10.1083/jcb.201211113

Rumpf, C., L. Cipak, A. Schleiffer, A. Pidoux, K. Mechtler, I.M. Tolić-Nørrelykke, and J. Gregan. 2010. Laser microsurgery provides evidence for merotelic kinetochore attachments in fission yeast cells lacking Pcs1 or Clr4. *Cell Cycle.* 9:3997–4004. http://dx.doi.org/10.4161/cc.9.19.13233

Santaguida, S., and A. Musacchio. 2009. The life and miracles of kinetochores. *EMBO J.* 28:2511–2531. http://dx.doi.org/10.1038/emboj.2009.173

Shimamoto, Y., Y.T. Maeda, S. Ishiwata, A.J. Libchaber, and T.M. Kapoor. 2011. Insights into the micromechanical properties of the metaphase spindle. *Cell.* 145:1062–1074. http://dx.doi.org/10.1016/j.cell.2011.05.038

Sikirzhytski, V., V. Magidson, J.B. Steinman, J. He, M. Le Berre, I. Tikhonenko, J.G. Ault, B.F. McEwen, J.K. Chen, H. Sui, et al. 2014. Direct kinetochore-spindle pole connections are not required for chromosome segregation. *J. Cell Biol.* 206:231–243. http://dx.doi.org/10.1083/jcb.201401090

Stephens, A.D., J. Haase, L. Vicci, R.M. Taylor II, and K. Bloom. 2011. Cohesin, condensin, and the intramolecular centromere loop together generate the mitotic chromatin spring. *J. Cell Biol.* 193:1167–1180. http://dx.doi.org/10.1083/jcb.201103138

Stephens, A.D., C.W. Quammen, B. Chang, J. Haase, R.M. Taylor II, and K. Bloom. 2013. The spatial segregation of pericentric cohesin and condensin in the mitotic spindle. *Mol. Biol. Cell.* 24:3909–3919. http://dx.doi.org/10.1091/mbc.E13-06-0325

Sun, M., R. Kawamura, and J.F. Marko. 2011. Micromechanics of human mitotic chromosomes. *Phys. Biol.* 8:015003. http://dx.doi.org/10.1088/1478-3975/8/1/015003

Tolić-Nørrelykke, I.M., L. Sacconi, G. Thon, and F.S. Pavone. 2004. Positioning and elongation of the fission yeast spindle by microtubule-based pushing. *Curr. Biol.* 14:1181–1186. http://dx.doi.org/10.1016/j.cub.2004.06.029

Uchida, K.S., K. Takagaki, K. Kumada, Y. Hirayama, T. Noda, and T. Hirota. 2009. Kinetochore stretching inactivates the spindle assembly checkpoint. *J. Cell Biol.* 184:383–390. http://dx.doi.org/10.1083/jcb.200811028

Umbreit, N.T., M.P. Miller, J.F. Tien, J.C. Ortolá, L. Gui, K.K. Lee, S. Biggins, C.L. Asbury, and T.N. Davis. 2014. Kinetochores require oligomerization of Dam1 complex to maintain microtubule attachments against tension and promote biorientation. *Nat. Commun.* 5:4951. http://dx.doi.org/10.1038/ncomms5951

Cojoc et al., http://www.jcb.org/cgi/content/full/jcb.201506011/DC1

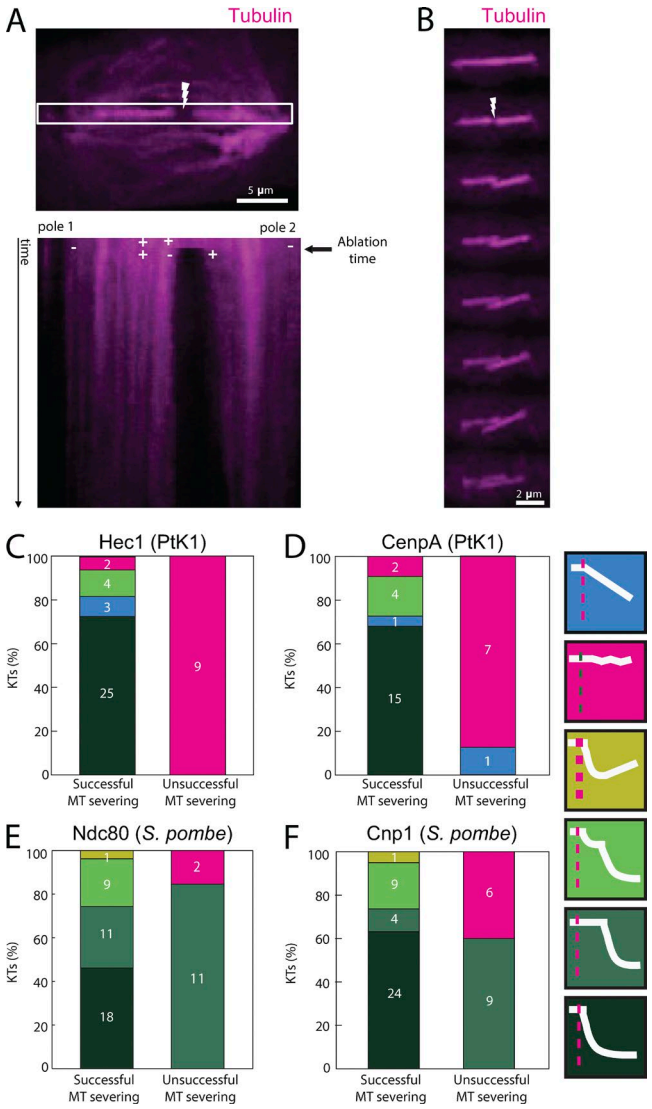

Figure S1. **Indications of successful MT severing in PtK1 and fission yeast cells and KT behavior observed after successful or unsuccessful MT severing.** (A) A PtK1 spindle is shown in the top image. The white lightning sign indicates the ablation site. The white rectangle indicates the area used to generate the time projection in the bottom image. The plus and minus end of the MT bundles are marked with white mathematical signs. After the ablation new plus and minus ends are created, and the region between the newly created MT ends increases in size because of plus-end depolymerization. Depolymerization of MT plus ends at the site of ablation is an indication of successful MT severing in PtK1 cells. (B) After ablation of the *S. pombe* spindle (indicated by white lightning sign), spindle breakage is observed. (C and D) PtK1 outer and inner KTs, respectively. (E and F) *S. pombe* outer and inner KTs, respectively. All panels are divided in two categories: successful severing and unsuccessful severing (only bleaching of the MTs occurred). Each category is divided according to observed phenotypes. On the right, schematic of observed phenotypes, from bottom to top: KTs shortened fast in a single step immediately after ablation (the most frequent phenotype), delayed shortening (KT shortening started more than 50 s after laser ablation), KTs shortened in two steps, KTs shortened initially but restretched later on, KTs that did not change their shape, and KTs that shortened in a very slow linear manner. Red dashed line indicates the ablation time.

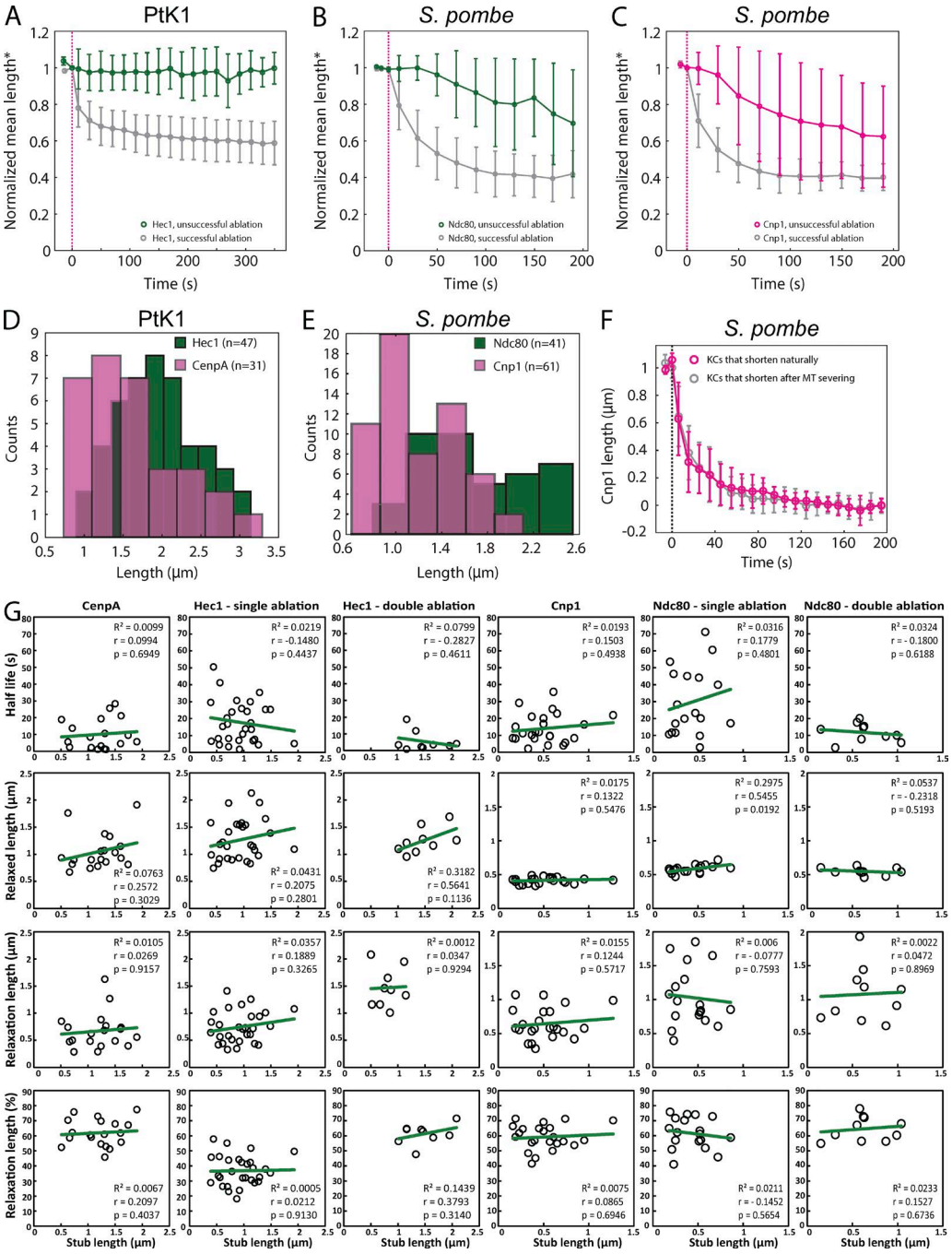

Figure S2. **Normalized KT length observed after successful or unsuccessful MT severing, comparison of outer KT and inner KT/centromere stretch, kinetics of relaxation for KTs that were repaired spontaneously, and effect of MT stub length on KT relaxation.** Normalized KT length as a function of time, for the outer KT in PtK1 (A), the outer KT in *S. pombe* (B), and the inner KT in *S. pombe* (C) are shown. For unsuccessful ablation, outer KT, Hec1/Ndc80, is shown in green and inner KT, Cnp1, in magenta. Gray curves are the relaxation kinetics for successful ablations in each case. Normalized mean length* represents data for each KT normalized by setting the value before the ablation to 1. Error bars represent standard deviation. (D and E) The outer KT is stretched more than the inner KT. Stretched KT length distributions for PtK1 (D) and *S. pombe* (E) are shown. For each KT, the stretched length was calculated as a mean of measured KT length before laser ablation. (F) The relaxation kinetics of the KTs that were repaired spontaneously are similar to those where the relaxation was induced by MT severing. Normalized kinetochore length as a function of time for the inner KT in *S. pombe* is shown. Relaxation kinetics of the KTs that shortened immediately after ablation is shown in gray. Relaxation kinetics of KTs that were naturally repaired is shown in magenta. The mean length of merotelic KTs naturally repaired was obtained by aligning the traces to the first frame before relaxation started. Data for each KT were normalized by setting the value before ablation to 1 and the minimum value to 0, binned, and averaged. Error bars represent standard deviation. G is organized as follows: graphs on each line represent the correlation, for all subdomains and systems, between the MT stub length and the half-life of the relaxation, relaxed length, absolute or relative relaxation length. Each line corresponds to a specific KT subdomain and/or system. MT stub length was defined as the distance between the ablation site and the KT. Relaxed length was defined as in Fig. 3. Relaxation length was defined as the amount that KT shortens upon ablation. The fitting curve is shown in green. Statistical analysis, goodness of the fit R^2, correlation coefficient *r*, and p-value for testing the hypothesis of no correlation are shown for each graph as an inset.

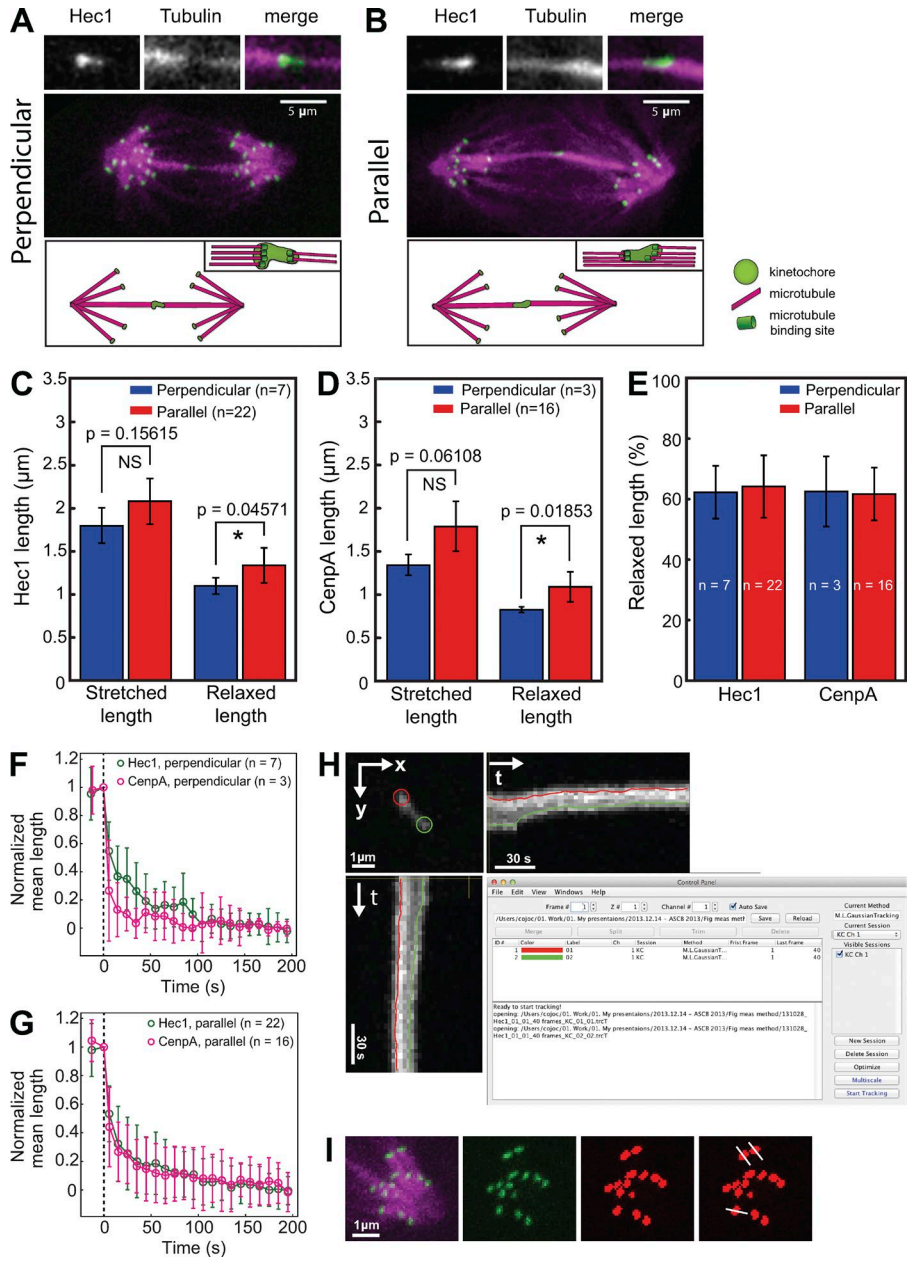

Figure S3. **Comparison of relaxation response of KTs with perpendicular or parallel MT attachments and a scheme of KT tracking.** (A and B) Images and corresponding drawings representing the two types of attachments: perpendicular and parallel. Bar, 5 µm; close up, 2×. Close-up views (2× magnification) of lagging KTs are shown on the top. (C and D) Comparison of the perpendicular versus parallel attachment. Bars are mean values of stretched and relaxed length of the KT in Hec1-GFP and GFP-CenpA PtK1 cells. Error bars represent standard deviation (NS, $P > 0.05$; *, $P < 0.05$). (E) Relaxed length as a percentage of the stretched length for both outer (Hec1) and inner (CenpA) KT and both parallel and perpendicular attachment types. (F and G) Normalized KT length as a function of time, for both the inner (magenta) and outer (green) PtK1 KT. Perpendicular (F) and parallel (G) attachments are shown. Data for each KT were normalized setting the value before ablation to 1 and the minimum value reached by the individual KT to 0, binned, and averaged. Error bars represent standard deviation. A stretched KT is shown in H (top left). Red and green circles indicate coordinates of the KT ends. Time projections along the x and y axes are shown in the top right and bottom left images, respectively. A screen shot of the software graphical interface used for tracking the KT ends is shown in the bottom right. (I) The first image shows control KTs (green) and K-fibers (magenta) from PtK1 cells expressing Hec1-GFP and injected with α-tubulin–X-rhodamine. The second image shows KT signal only (green). The third image shows segmented image of the KT signal. Three white lines in the fourth image indicate measured KTs and the direction of the measurement.

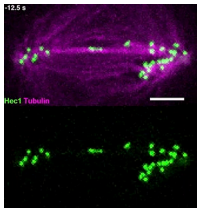

Video 1. **Single ablation in PtK1 cells expressing Hec1-GFP.** (top) Live-cell microscopy of a PtK1 mitotic cell and the severing of one of the two K-fibers. The cell expressing Hec1 labeled with GFP (green) was injected with α-tubulin-X-Rhodamine (magenta). Images were acquired at 2.5-s intervals. The video is displayed at 10 fps. Bar, 5 µm. The video corresponds to Fig. 1 B. (bottom) Separate green channel showing PtK1 KTs (Hec1-GFP).

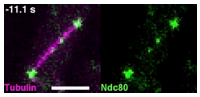

Video 2. **Single ablation in *S. pombe* cells expressing Ndc80-GFP.** (left) Live-cell microscopy of a *S. pombe* mitotic cell and the severing of the spindle. The cell expressing Ndc80 labeled with GFP (green) and α-tubulin labeled with mCherry (magenta) is shown. Images were acquired at 2.8-s intervals. The video is displayed at 10 fps. Bar, 3 µm. The video corresponds to Fig. 1 E. (right) Separate green channel showing *S. pombe* KTs (Ndc80-GFP).

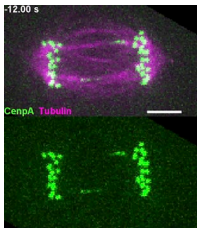

Video 3. **Single ablation in PtK1 cells expressing GFP-CenpA.** (top) Live-cell microscopy of a PtK1 mitotic cell and the severing of one of the two K-fibers. The cell expressing CenpA labeled with GFP (green) was injected with α-tubulin–X-rhodamine (magenta). Images were acquired at 2.4-s intervals. The video is displayed at 10 fps. Bar, 5 µm. The video corresponds to Fig. 2 A. (bottom) Separate green channel showing PtK1 KTs (GFP-CenpA).

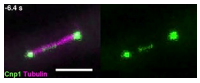

Video 4. **Single ablation in *S. pombe* cells expressing Cnp1-GFP.** (left) Live-cell microscopy of a *S. pombe* mitotic cell and the severing of the spindle. The cell expressing Cnp1 labeled with GFP (green) and α-tubulin labeled with mCherry (magenta) is shown. Images were acquired at 3.2-s intervals. The video is displayed at 10 fps. Bar, 3 µm. The video corresponds to Fig. 2 D. (right) Separate green channel showing *S. pombe* KTs (Cnp1-GFP).

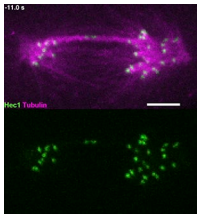

Video 5. **Double ablation in PtK1 cells expressing Hec1-GFP.** (top) Live-cell microscopy of a PtK1 mitotic cell and the severing of one of both K-fibers. The cell expressing Hec1 labeled with GFP (green) was injected with α-tubulin–X-rhodamine (magenta). Images were acquired at 2.2-s intervals. The video is displayed at 10 fps. Bar, 5 µm. The video corresponds to Fig. 3 A. (bottom) Separate green channel showing PtK1 KTs (Hec1-GFP).

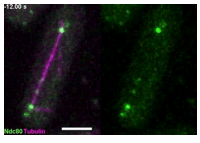

Video 6. **Double ablation in *S. pombe* cells expressing Ndc80-GFP.** (left) Live cell microscopy of a *S. pombe* mitotic cell and the severing of the spindle. The cell expressing Ndc80 labeled with GFP (green) and α-tubulin labeled with mCherry (magenta) is shown. Images were acquired at 3-s intervals. The video is displayed at 10 fps. Bar, 3 µm. The video corresponds to Fig. 3 D. (right) Separate green channel showing *S. pombe* KTs (Ndc80-GFP).

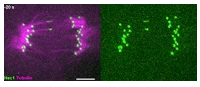

Video 7. **PtK1 cells expressing Hec1-GFP treated with NOC.** (left) Live-cell microscopy of a PtK1 mitotic cell treated with NOC. The cell expressing Hec1 labeled with GFP (green) was injected with α-tubulin–X-rhodamine (magenta). Time 0 indicates the frame before addition of 9 µM NOC. Images were acquired at 20-s intervals. The video is displayed at 10 fps. Bar, 5 µm. The video corresponds to Fig. 3 G. (right) Separate green channel showing PtK1 KTs (Hec1-GFP).